Joule

CellPress

Article

Exploiting Electrical Transients to Quantify Charge Loss in Solar Cells

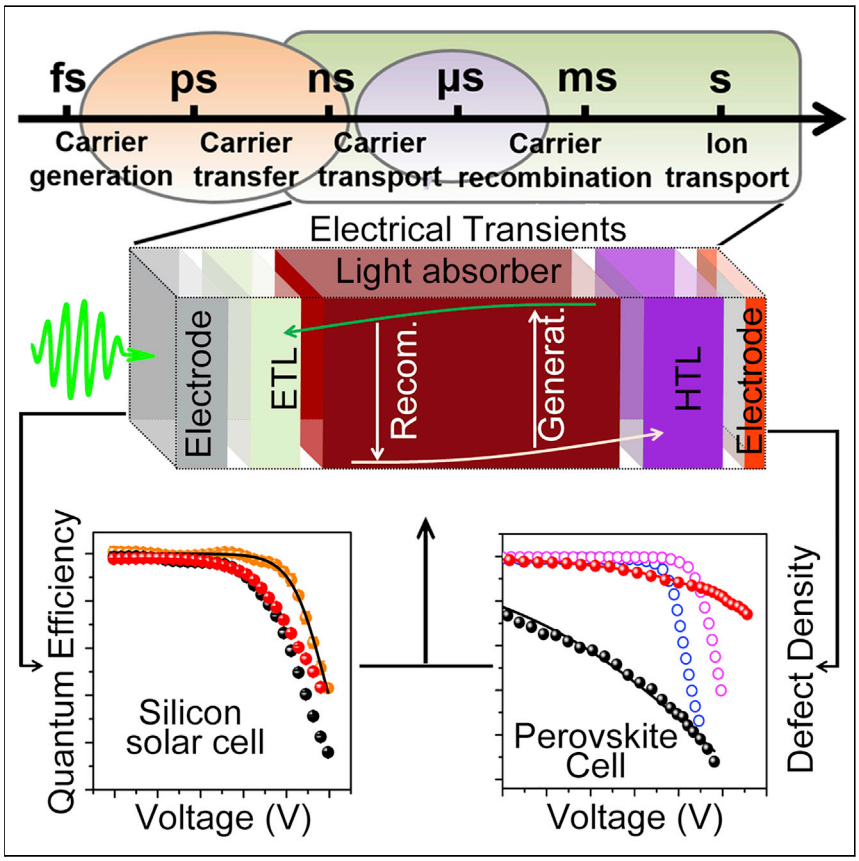

Junction solar cells are the largest members of the photovoltaic society. Herein, a new analysis methodology of electrical transients has been presented to quantitatively extract charge dynamics properties and charge loss mechanisms of these devices. This methodology has been successfully applied to study conventional silicon and emerging $Cu_2ZnSn(S, Se)_4$ and perovskite solar cells and is able to extend to other photovoltaic device systems, thus exhibiting important implications for the characterization investigations of energy conversion devices.

Yiming Li, Jiangjian Shi, Bingcheng Yu, ..., Yanhong Luo, Huijue Wu, Qingbo Meng

qbmeng@iphy.ac.cn

HIGHLIGHTS

New understanding on electrical transients of solar cells is presented

New methodology for electrical transient analysis is established

Charge dynamics properties and charge loss of solar cells are quantified

Li et al., Joule 4, 472–489
February 19, 2020
https://doi.org/10.1016/j.joule.2019.12.016

Joule

CellPress

Article

Exploiting Electrical Transients to Quantify Charge Loss in Solar Cells

Yiming Li,[1,3,5] Jiangjian Shi,[1,5] Bingcheng Yu,[1,3] Biwen Duan,[1,3] Jionghua Wu,[1,3] Hongshi Li,[1,3] Dongmei Li,[1,3,4] Yanhong Luo,[1,3,4] Huijue Wu,[1] and Qingbo Meng[1,2,4,6,*]

SUMMARY

Electrical transients enabled by an optical excitation and an electric detection provide a distinctive opportunity to study charge transport, recombination, and even photoelectric hysteresis of a solar cell in a wide time window ranging from nanoseconds to seconds. However, controversies on how to exploit these investigations to unravel the charge loss mechanism of the cell have been ongoing. Herein, a new methodology of quantifying the charge loss within the bulk absorber or at the interfaces and the defect properties of solar cells has been proposed. This methodology has been successfully applied in the study of commercialized silicon and emerging $Cu_2ZnSn(S, Se)_4$ and perovskite solar cells herein and should also be applicable to other similar photovoltaic device systems. Overall, this work provides an alluring route for a comprehensive investigation of dynamic physics processes and charge loss mechanism of solar cells and possesses potential applications for other optoelectronic devices.

INTRODUCTION

Functionalization of a semiconductor device, such as a photovoltaic, integrated circuit etc., is mainly enabled by optical-electrical or electrical-electrical interconversions, which is intrinsically dominated by internal charge-carrier processes.[1–4] Recently, hybrid lead halide perovskite, which exhibits outstanding optical-electrical conversion abilities, has been identified to possess abundant charge-carrier characteristics, such as slow hot carrier cooling,[5–8] long polarization memory,[9–11] and fast ion migrations.[12–15] These novel photophysical behaviors significantly enrich the semiconductor family and have spawned a new discipline, that is, perovskite optoelectronics. Probing and manipulating these processes provide an effective route for improving the material performance and extending the perovskite application.

For the perovskite solar cell, steady-state energy conversion is realized only after experiencing a variety of processes including charge generation, charge transfer and transport within the bulk absorber and the charge transporting layers (CTLs), charge recombination at the bulk and interface, and even photoelectric hysteresis.[16] A series of optical and electrical transient methods have been exploited to probe these dynamic processes in a wide time span ranging from sub-picoseconds to even hours to shed light on the working and charge loss mechanisms of this emerging material and cell.[17–37] Compared to the advanced ultrafast optics measurements,[17–29] perturbation electrical transients (e.g., transient photocurrent [TPC] and photovoltage [TPV])[30–37] enabled by an optical excitation and an electric detection provide an opportunity to study charge transport, recombination, and even the hysteresis in a much wider time window. This technique has been widely

Context & Scale

Functionalization of a semiconductor device, such as photovoltaic and integrated circuits, is mainly enabled by optical-electrical or electrical-electrical interconversions. The energy conversion of a semiconductor solar cell is realized only after experiencing a variety of charge processes. Understanding, probing, and manipulating these processes form the foundation for material and device performance improvements. Electrical transients comprised of optical excitations, and electric detections provide opportunities to probe charge transport, recombination, and even photoelectric hysteresis of the cell in wide time windows. Herein, a new analysis methodology of electrical transients has been established to quantitatively extract charge dynamics properties and charge loss of junction solar cells. This methodology helps better understand the device physics of emerging solar cells and brings an alluring approach for the characterization and investigation of solar cells.

applied for silicon,[38,39] sensitized,[40,41] quantum dot,[42] organic,[43] and recently the perovskite solar cells.[30–35]

A generic physics model and quantitative analysis method centered on the charge occupation of subgap tail states has been extended from sensitized solar cells to current perovskite solar cells.[31,32,44–46] Within this model, the distribution of tail states has been interpreted as a common origin for the difference in the device performance and especially the open-circuit voltage, no matter the device structure and working mechanism. This raises several fundamental questions, which are (1) do all the cells follow the same electrical transient processes or charge loss mechanism? (2) Can the electrical transients be used to reflect the distribution of tail states or subgap states? (3) What does the electrical transient measurement really tell us?

Controversies on electrical transient behaviors of solar cells have always been ongoing. For instance, Marlow et al. doubted whether the charge transport in dye-sensitized solar cells had been really understood, according to their voltage-dependent photocurrent measurement.[47] Recently, Tvingstedt et al. also proposed a new understanding on the charge lifetime that derived from the electrical transients of a variety of thin film photovoltaic devices.[30] For the perovskite solar cell, whether the measured tail states arise from the bulk perovskite or from the charge transporting layer is also under controversy.[48–50] Therefore, understanding the device physics truth from the electrical transients and exploiting these approaches to unravel the charge loss mechanism of solar cells, especially of the emerging perovskite solar cell, should be an important research topic for the photovoltaic field.

In this work, we propose a new analysis methodology to quantitatively extract charge dynamics properties and charge loss mechanism of photovoltaic devices (such as charge extraction and collection quantum efficiency and the density of defects within the absorber) from the electrical transients. This methodology has been successfully applied to study conventional silicon and emerging Kesterite and perovskite solar cells herein and is able to extend to other similar photovoltaic device systems. Therefore, this work provides an alluring route for a comprehensive investigation of dynamic physics processes and charge loss mechanism of solar cells and possesses potential applications for other optoelectronic devices.

For clarity, in this paper we will first focus on the differential capacitance of devices and discuss the validity of conventional tail-state framework. Then, the carrier dynamics and charge loss mechanism behind electrical transients will be further studied based on theoretical calculations. Finally, we will propose a new analysis methodology and self-consistent physics model to quantify charge loss and defect density by electrical transients, which is proved to be applicable for a series of junction solar cells. Notably, all the discussions in this work are limited within the perturbation electrical transient analysis, which may be different from other methods that significantly deviate from the quasi steady state.

RESULTS

Figure 1A gives a schematic diagram of general charge-carrier processes within a perovskite solar cell where the perovskite absorber (PVSK) is sandwiched by electron (ETL) and hole transporting layers (HTL). Sn: In_2O_3 (ITO) and Au are used as the front and back electrodes to collect electrons and holes from the ETL and

[1]Key Laboratory for Renewable Energy, Beijing Key Laboratory for New Energy Materials and Devices, Institute of Physics, Chinese Academy of Sciences, Beijing 100190, P. R. China

[2]Center of Materials Science and Optoelectronics Engineering, University of Chinese Academy of Sciences, Beijing 100049, China

[3]School of Physics Science, University of Chinese Academy of Sciences, Beijing 100049, P. R. China

[4]Songshan Lake Materials Laboratory, Dongguan, Guangdong 523808, China

[5]These authors contributed equally

[6]Lead Contact

*Correspondence: qbmeng@iphy.ac.cn

https://doi.org/10.1016/j.joule.2019.12.016

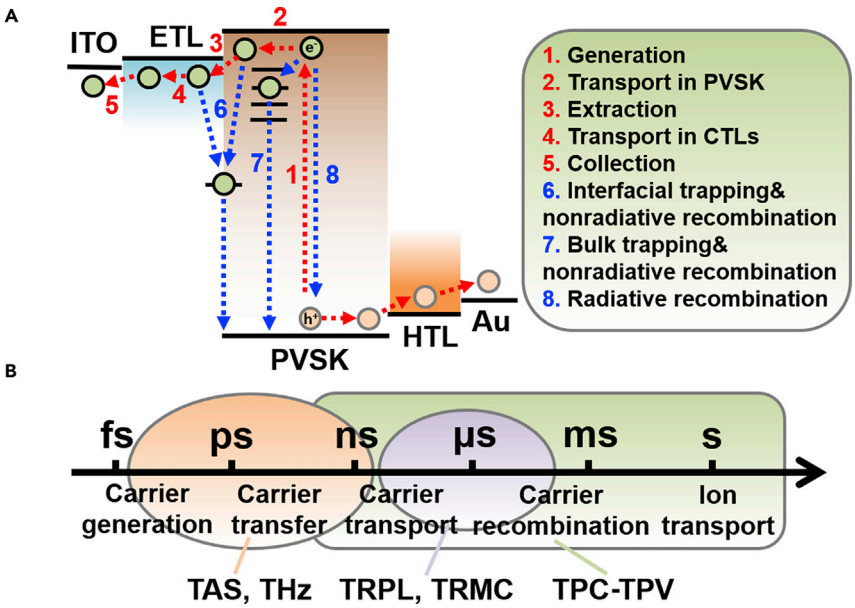

Figure 1. General Charge-Carrier Processes within a Perovskite Solar Cell

(A and B) Carrier dynamics processes (A) and the corresponding time scale of the cell (B). Different transient technologies including transient absorption spectroscopy (TAS),[17,18] terahertz pump-probe technology (THz),[19–21] time-resolved photoluminescence (TRPL),[22–26] microwave photo-conduction (TRMC),[27–29] and TPC-TPV measurements[30–37] have been used to probe these carrier dynamic processes.

HTL, respectively. To produce electricity, the photon-generated charges need to experience transportation in the PVSK, extraction at the ETL and HTL-perovskite interfaces, and collection at the electrode interfaces. Due to the bulk and interface defects, charge loss is usually unavoidable. The cell performance is ultimately determined by the dynamic competition between charge transport-extraction-collection and charge loss due to recombination. As shown in Figure 1A, these processes occur in a wide time span ranging from nanosecond to millisecond, which is exactly within the detection window of electrical transients.[17–37] Therefore, electrical transient is expected to be a powerful approach to reveal charge loss mechanisms of a solar cell.

Tail-State Framework–Differential Capacitance

Conventionally, the charge loss mechanism of a solar cell derived from the TPC-TPV analysis is explored within the framework of tail state distribution.[31,32] For this framework, the variation in the device performance and especially in the open-circuit voltage (V_{OC}) is mainly attributed to the tail (or subgap) state distribution, which is usually reflected by the stored charge (Q (V_{OC})) at the open-circuit condition. The Q (V_{OC}) is obtained by integrating the differential capacitance (C_{DC}) of the cell, and the C_{DC} is determined by the TPC-TPV method, that is:

$$C_{DC}(V_{OC}) = \Delta Q(V_{OC})/\Delta V(V_{OC}) \approx \Delta Q(I_{OC})/\Delta V(V_{OC}), \quad \text{(Equation 1)}$$

where ΔV is the TPV peak at different V_{OC}, ΔQ is the perturbation charge integrated from the TPC decay at different light illumination intensity (I_{OC}) corresponding to the V_{OC}.

Generally, ΔV is measured in the open-circuit (OC) condition while ΔQ is measured in the short-circuit (SC) condition. An assumption has been made to make Equation 1

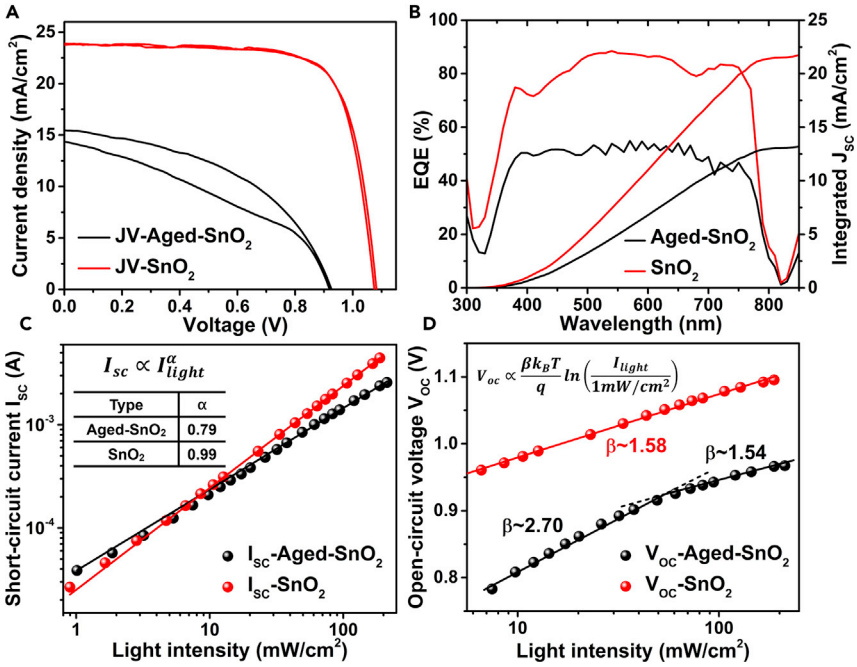

Figure 2. Current-Voltage (*I-V*) and Charge Recombination Properties of the Studied Cells

(A) Representative *I-V* curves of the SnO_2-based perovskite solar cell without or with experiencing time aging.

(B) EQE spectra of the cells.

(C and D) Light intensity-dependent (C) short-circuit current (I_{SC}) and (D) open-circuit voltage (V_{OC}).

applicable, that is, the difference of ΔQ (I_{OC}) to the ΔQ (V_{OC}) can be ignored. Based on this assumption, this framework was widely used for the sensitized and organic solar cells and has been extended to the perovskite solar cells.[31,32,44–46] In the following section, we will first check the validity of this assumption based on the C_{DC} measurement of perovskite solar cells.

A perovskite solar cell with a configuration of ITO-SnO_2-PCBA-perovskite-Spiro OMeTAD-Au was used as the standard sample, which gives a power conversion efficiency (PCE) of 19.2% with negligible hysteresis behavior. The PCBA was used here as an interface passivation layer, which can help significantly suppress the interface defect.[51,52] With this passivation, no signature of severe interface recombination (e.g., fast early-stage TPV decay) was observed in our experiment. Thus, possible charge loss and bending of quasi-Fermi-energy-level splitting at interfaces are not considered in this work.[53] Another sample with a significantly degraded PCE of ~7% was obtained by aging the standard cell for several months in ambient conditions. Notably, phase segregation of the perovskite absorber, which could obviously degrade the cell,[54] did not appear in our aged sample. Thus, we infer that the efficiency degradation here mainly arises from the variations of the defect and charge recombination properties. Figures 2B–2D give bias light-intensity-dependent SC current and V_{OC} characterizations of these two cells to further evaluate the degradation mechanism. The α values of the fitted line for aged-SnO_2 and SnO_2 devices presented in Figure 2C are 0.79 and 0.99, respectively, indicating that the aged-SnO_2 device exhibits a higher recombination loss under short-circuit conditions.[55] In Figure 2D, the obtained β of the SnO_2 device is around 1.6, which is consistent with previous results.[56] For the aged-SnO_2 device, the β is higher than 2.0 when the light intensity is lower than 60 mW cm^{-2}, suggesting a higher defect

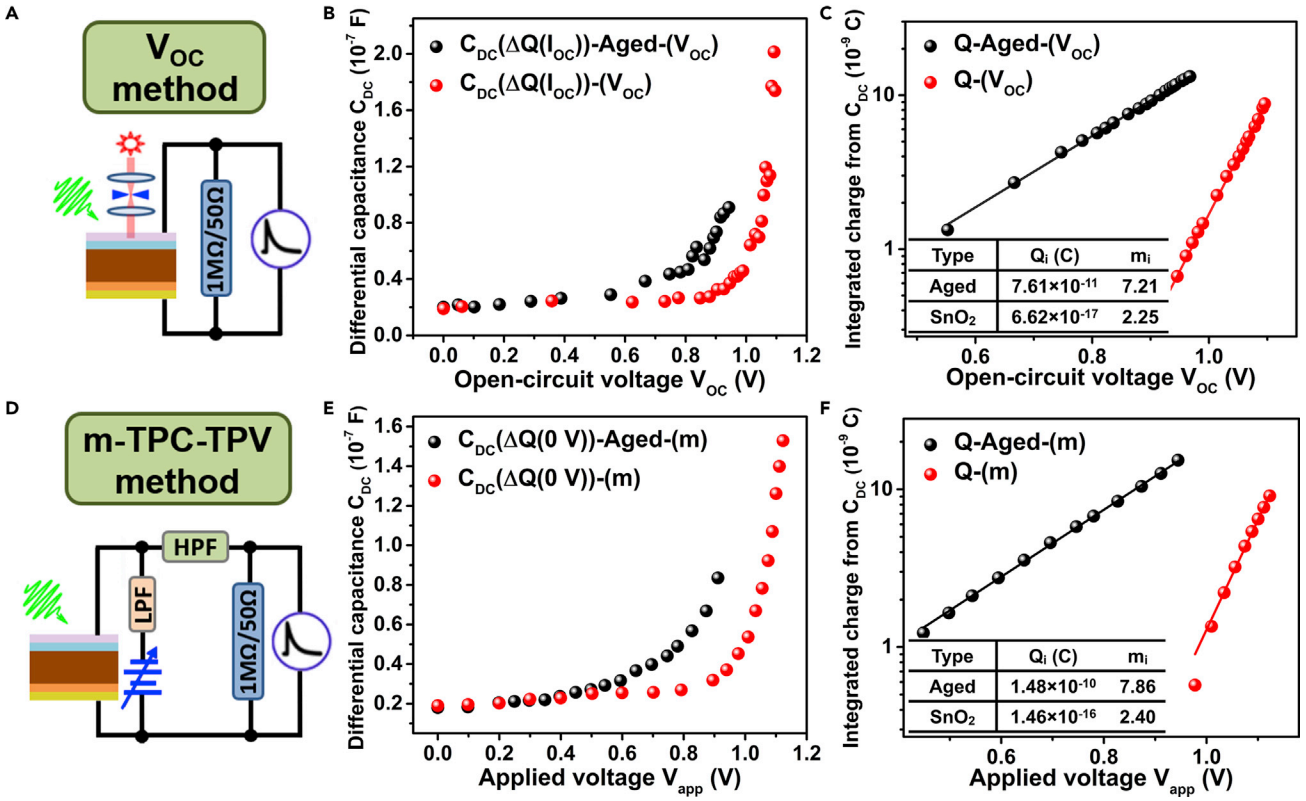

Figure 3. Evaluating the Tail State of the Cell within the Conventional Framework

(A) Schematic diagram of the V_{OC}-TPC-TPV measurement. An LED with adjustable light intensity is used to produce the steady-state V_{OC} voltage bias.

(B) Differential capacitance C_{DC} as a function of V_{OC} for the aged-SnO_2 and SnO_2 devices.

(C) Total integrated charge density Q as a function of V_{OC}.

(D) Schematic diagram of the designed m-TPC-TPV system. A steady-state voltage source is used to give bias voltage to the cell and a high-pass filter (HPF) together with a low-pass filter (LPF) is applied to separate the transient electrical signal from the voltage source to avoid shunting.

(E) C_{DC} as a function of applied voltage V_{app} for the cells.

(F) Q in two devices as a function of V_{app}. All the theoretical fittings were made within the conventional tail-state framework.

recombination loss. At higher light intensity, the β decreases to 1.5. This reduction of β suppresses the increase trend of V_{OC}, which may be caused by an additional non-radiative recombination loss and insufficient contact selectivity at high light intensities.[57]

We first use the conventional tail state scenario and Equation 1 to evaluate the C_{DC} and thus to compute the stored charge ($Q(V_{OC})$) within the cell (especially within the tail states) under varied V_{OC} by an integration of the C_{DC}, that is:

$$Q(V_{OC}) = \int_0^{V_{OC}} (C_{DC} - C_{electrode})dV, \qquad \text{(Equation 2)}$$

where $C_{electrode}$ is the electrode or geometry capacitance determined from the flat baseline of C_{DC} at low V_{OC}.

This V_{OC}-TPC-TPV measurement scheme is shown by Figure 3A, where the TPC is measured with a 50 Ω sampling resistor and TPV is measured with a 1 MΩ sampling resistor. Figures 3B and 3C give the C_{DC} and integrated Q results, which agree well with the previous scenario with an exponential distribution feature.[31] The tail state

properties of the perovskite was believed to be able to be parameterized by fitting the distribution of Q as:

$$Q(V_{OC}) = Q_i \exp\left(\frac{qV_{OC}}{m_i K_B T}\right), \quad \text{(Equation 3)}$$

where q is the elementary charge, K_B is the Boltzmann constant, T is the absolute temperature, and Q_i and m_i are the fitting factors which are usually used to reflect the effective density of states of the tail state.

Clearly, a degraded sample gives a much larger Q_i, which was believed to indicate a much higher tail state density according to the conventional scenario. This interpretation seems reasonable because higher tail-state density can indeed lead to more severe charge recombination and lower cell efficiency.

In fact, besides the bias light-induced V_{OC}, we can also adjust the electric properties of the cell by directly applying a paralleled-connected external voltage source. To avoid the influence of this voltage source on the TPC-TPV detecting, a low-pass filter (LPF) is used to separate the high-frequency transient signal, as shown in Figure 3D, which has led to a realization of instrument design of modulated TPC-TPV (m-TPC-TPV), as we once reported.[33] By using $C_{DC}(V_{app}) \approx \Delta Q(0\,V)/\Delta V(V_{app})$, where V_{app} is the applied bias voltage, a similar result to that of tail state scenario was obtained, as shown in Figures 3E and 3F. This indicates that V_{OC} plays a similar role to the V_{app} in influencing the cell electronic properties and more importantly that our previous instrument design itself cannot bring new insight into the characterization of electrical transient and charge loss mechanism of solar cells if still following the conventional analysis scenario.

To obtain a deep understanding of the conventional scenario and the derived exponential C_{DC}-V_{OC} relationship (Figure 3), we need to accurately measure the $\Delta Q(V_{OC})$ to check the validity of Equation 1. By introducing a high-pass filter (HPF) in the V_{OC}-TPC-TPV measurement system, we can measure the TPC signal even when the cell works in the steady-state OC condition, as schematically shown in Figures 4A and 4B. The TPC of the standard and degraded cells at a series of V_{OC} (measurement scheme in Figure 4B) and V_{app} (measurement scheme in Figure 3D) were measured to obtain the $\Delta Q(V_{OC})$ and $\Delta Q(V_{app})$, respectively. The obtained $\Delta Q(I_{OC})$ (measurement scheme in Figure 4A) results are also presented in Figures 4C and 4E for a direct comparison. No matter the V_{OC} or the V_{app} mode, the ΔQs exhibit an obvious decrease at a high voltage whereas the $\Delta Q(I_{OC})$ is almost constant. This means that the widely used approximation $\Delta Q(V_{OC}) \approx \Delta Q(I_{OC})$ is not valid in experiments, at least for our cells studied here. Further with the TPV peaks (i.e., $\Delta V(V_{OC})$ and $\Delta V(V_{app})$) presented in Figures 4D and 4F, the C_{DC} of the cells is recalculated and shown in Figure 4G (see Experimental Procedures). It can be seen that the exponential feature only appears when the above inaccurate approximation is used. Without using this artificial approximation, the C_{DC} is almost constant in the whole voltage region, whatever the measurement mode. In this case, the analysis of tail state distribution through Equation 3 is not valid any more. In addition, no difference in the C_{DC} was observed for these two cells although they exhibited obviously different carrier recombination characteristics. Thus, the applicability of the widely used tail state framework for the cell electrical transient characterization, especially for the perovskite and other junction solar cells, needs be reconsidered.

Carrier Dynamics and Charge Loss Mechanisms behind Electrical Transients

To have a deep insight into the above clarification, two more fundamental questions about the electrical transient process of a solar cell will be unraveled here, that is, (1)

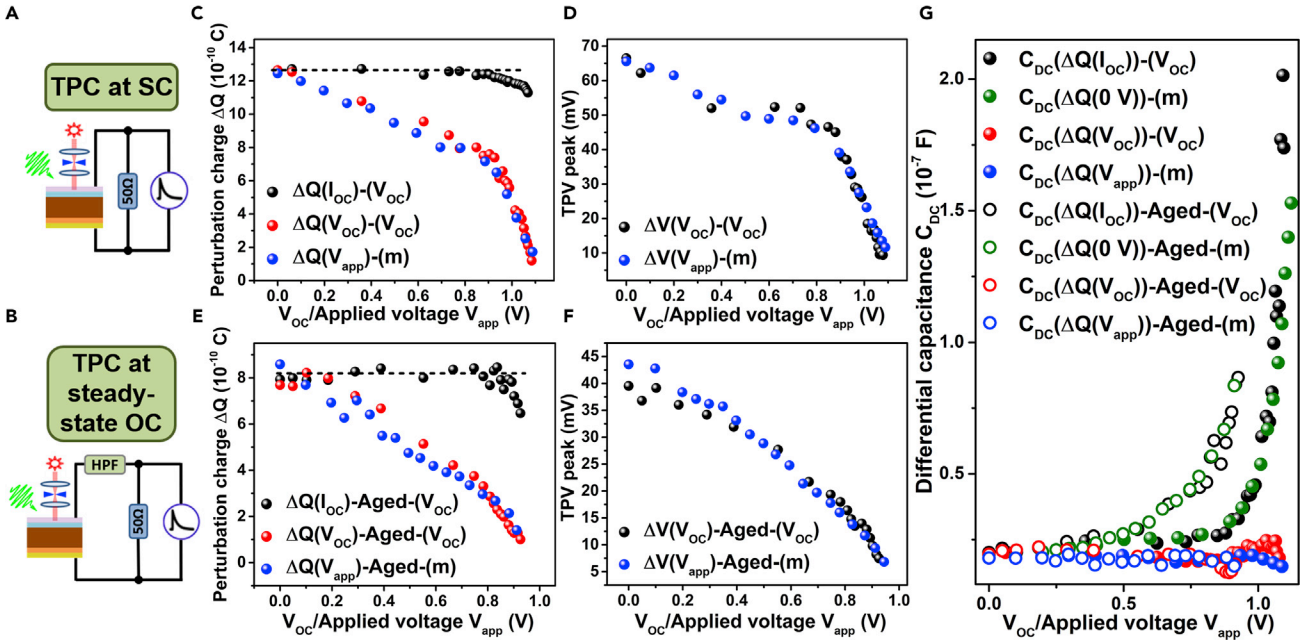

Figure 4. Accurate Measurement of the C_{DC}

(A–F) Schematic diagrams of perturbation charge measurement using (A) the conventional V_{OC}-TPC-TPV system or (B) a modified V_{OC}-TPC-TPV system by introducing an HPF, which can help measure the TPC when the cell works under a steady-state OC condition. Integrated charge ΔQ (I_{OC}) (black sphere), ΔQ (V_{OC}) (red sphere) and ΔQ (V_{app}) (blue sphere) for the SnO_2 and aged-SnO_2 device, and comparisons of the TPV peak ΔV (V_{OC}) (black sphere) and ΔV (V_{app}) (blue sphere) of these two cells (C ΔQ and D ΔV of the SnO_2 cell, E ΔQ and F ΔV of the aged-SnO_2 cell).

(G) C_{DC} of these two cells computed from different methods (see Experimental Procedures). The conventional method gives an exponential behavior while a more accurate measurement of the perturbation charge yields a constant C_{DC} across the whole voltage regimen. No difference in the C_{DC} can be observed between these two cells.

how the charge loss within the cell influences the TPC and TPV, and (2) when and how the photovoltage is established.

The photo-generated charge (ΔQ_{tot}) can be divided into four parts at the time point of TPV peak, that is:

$$\Delta Q_{tot} = \Delta Q_{ext}(V_{app}) + \Delta Q_{R}(V_{app}) + \Delta Q_{TS}(V_{app}) + \Delta Q_{CB(VB)}(V_{app}), \qquad \text{(Equation 4)}$$

where ΔQ_{ext} is the extracted charge that located at the ETL and HTL-perovskite interfaces, ΔQ_R is the charge lost due to bulk recombination, ΔQ_{TS} is the charge that is located in the tail state, and $\Delta Q_{CB/VB}$ is the charge that is still stored in the continuum conduction and valence band of the light absorber.

It is reasonable to assume that the charge trapping and detrapping velocity of the tail state is in the similar order of magnitude. Thus, at a certain steady-state condition, the sum of ΔQ_{ext}, ΔQ_{TS}, and $\Delta Q_{CB(VB)}$ can be estimated from the TPC integration. This sum is intrinsically determined by the charge loss item ΔQ_R (V_{app}). In the conventional framework, this charge loss item has rarely been considered. This neglect may be applicable for the sensitized solar cell, because the charge transfer from dye (quantum dot) to the charge transporting layers is usually ultrafast;[58–61] whereas for the perovskite and other junction solar cells, it should be unreasonable because this charge transfer process usually costs tens to hundreds of nanoseconds, in the similar time scale to that of bulk recombination.[16]

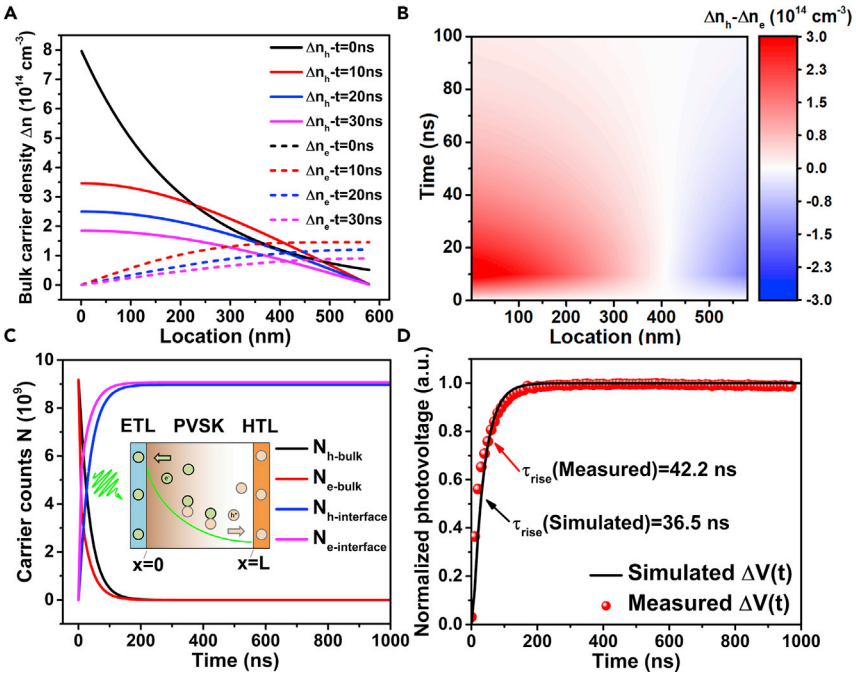

Figure 5. Simulation of the Charge Transport within the Perovskite Absorber and the Establishing Process of the Photovoltage

(A) The distributions of photo-generated electron $n_e(x, t)$ and hole $n_h(x, t)$ within the perovskite absorber at several time points.

(B) The contour plot of the net charge distribution within the perovskite absorber versus location and time.

(C) The time-dependent net charge within the perovskite and at the ETL and HTL interfaces. The inset is a schematic diagram of carrier transport processes within the diffusion model.

(D) A simulation of the photovoltage rise process (black line) and a typical experimental result (red sphere) obtained from TPV.

We will further demonstrate that the peak photovoltage is established only after the charge experiencing transfer and bulk recombination processes. The photovoltage of the cell is simulated using Poisson's equation,[2] that is:

$$\frac{\partial^2 V(x,t)}{\partial x^2} = -\frac{\rho(x,t)}{\epsilon}, \qquad \text{(Equation 5)}$$

where the time-dependent charge distribution $\rho(x, t)$ (i.e., $q(n_h(x, t)\text{-}n_e(x, t))$. n_h: hole density, n_e: electron density, x: position, t: time) within the cell is obtained by considering the carrier transport and bulk recombination processes.

Herein, the carrier drift behavior is ignored because the bulk electric field within the perovskite absorber has been significantly weakened by the ion migration.[62] Within the silicon solar cell, the width of the charge-neutral region (diffusion) is also much larger than that of the depletion region (drift). Due to the obvious difference in the carrier mobility between perovskite and the charge transporting layer, the extracted charge is considered locating at the interface with an approximated δ distribution with a total charge of ΔQ_{ext}.

The electron and hole distributions within the perovskite absorber at several time points are presented in Figure 5A (see Experimental Procedures). At the initial time, the electron and hole possess the same distribution, and thus no net charge exists within the cell. With carrier transport, the electron and hole are separated in

space due to their different boundary conditions. The resulting net charge distribution within the perovskite absorber is shown in Figure 5B. The time-dependent net charge within the perovskite and at the ETL and HTL interfaces is further calculated and presented in Figure 5C. After the charge transport and transfer for ~200 ns, all the net charges are located at the interface and charge loss due to the bulk recombination can be clearly seen.

According to Equation 5 and Figure 5B, the establishing behavior of the TPV is further derived by computing the time-dependent potential difference between the ETL and HTL, that is, $\Delta V = |V_{ETL} - V_{HTL}|$. The theoretical result is given in Figure 5D with a solid line, where the TPV peak appears at ~200 ns. At this time point, net charge is no longer stored within the bulk perovskite, but at the ETL and HTL interfaces, that is, $\Delta Q_{CB(VB)}$ approaches zero and ΔQ_{ext} reaches its maximum of $\sim(\Delta Q_{tot} - \Delta Q_R)$. For comparison, the TPV-rising behavior of the cell was also measured and presented. Clearly, the theoretical result agrees well with the experimental result, demonstrating the reasonability of the above discussions. These results provide unambiguous support for our first conclusion, that is, the charge loss arising from bulk recombination cannot be ignored when using the electrical transient characterizations. The decrease of ΔV (V_{app}) or ΔV (V_{OC}) at high voltages are mainly caused by the voltage-enhanced bulk recombination, which cannot be reflected by the C_{DC} feature because the C_{DC} performs more like an electrode or geometry capacitance. Notably, if the tail state has a great influence on the charge-carrier dynamics and distribution, the exponential C_{DC} and ΔQ_{TS} features may be observed again since the charge located in the tail state could also influence the charge distribution and thus the TPV peak. Honestly, this phenomenon has never been observed in our silicon and perovskite device experiments. For the sensitized or organic solar cell, this feature may be observed although it is beyond the discussion of this work. Nonetheless, it is still an open question whether the transferred perturbation charge from the light absorber can immediately generate peak photovoltage within these cells.

Quantification of Charge Loss and Defect Density by Electrical Transients

As the conventional framework is invalid more or less, a new way is urgently needed to quantify the charge loss and defect properties of the cell by using electrical transients. Here, for clarity, we deliberately separate the above charge-carrier dynamics into two processes, that is, (1) charge extraction at the perovskite interfaces and (2) charge collection at ETL and HTL-electrode interface. This dynamic separation is reasonable because they occur in an obviously distinct position and time scale. Extraction results from the carrier, transport within the perovskite absorber (~ tens of nanoseconds), whereas collection results from carrier, transport within the ETL and HTL (hundreds of nanoseconds to several microseconds).[16] During the extraction, charge loss occurs through the bulk recombination mechanism; whereas for the collection, charge losses occur through the backward recombination at the ETL and HTL-perovskite interfaces. We have previously demonstrated that the charge collection efficiency (η_C) can be derived from the TPC (τ_C) and TPV decay lifetime (τ_r), that is,[16,33]

$$\eta_C(V) = 1 - \tau_C(V)/\tau_r(V). \quad \text{(Equation 6)}$$

Under a reasonable assumption that the internal quantum efficiency (IQE) of a cell at −1 V is approaching the unity, the IQE of the cell at different voltages can be estimated as

$$\mathrm{IQE}(V) = \Delta Q(V)/\Delta Q(-1\ \mathrm{V}), \quad \text{(Equation 7)}$$

where the ΔQ is obtained from the TPC integration.

The introduction of Equation 7 can significantly improve the measurement accuracy compared to our previous route where the quantum efficiency was obtained by comparing the ΔQ and the perturbation light flux because there is great inaccuracy in measuring the weak light pulse flux. Gathering the η_C and IQE together, we can evaluate the charge extraction efficiency (η_{ext}) as,[33]

$$\eta_{ext}(V) = \mathrm{IQE}(V)/\eta_C(V). \quad \text{(Equation 8)}$$

These three quantum efficiencies were used to quantify the charge loss within the cell and to discriminate the space-related charge loss mechanism. Simply, a low η_{ext} (V) means a high charge recombination or inefficient charge transport within the light absorber, whereas a low η_C (V) implies the interfacial backward recombination needs to be suppressed. Nonetheless, with the m-TPC-TPV and these extracted efficiencies, we can only give a simple qualitative description of the charge loss within the cell. This fact demands us to further investigate device physics of solar cells to establish a new analysis methodology correlated to the electrical transients.

Having a closer look at the charge processes within the bulk absorber, the η_{ext} can be theoretically derived by considering the competition between charge transport and recombination within the absorber, that is:

$$\eta_{ext}(V) = \frac{\Delta Q_{ext}}{\Delta Q_{tot}} = \frac{\Delta Q_{ext}}{\Delta Q_{ext} + \Delta Q_R} = \frac{1}{1 + \frac{\tau_{ext}(V)}{\tau_R(V)}}, \quad \text{(Equation 9)}$$

where τ_{ext} is the effective transport time of carriers within the bulk absorber and τ_R is the carrier recombination lifetime.

According to the one-dimensional carrier diffusion model,[63] τ_{ext} can be estimated from the carrier diffusion coefficient (D) and the thickness of the bulk absorber (L), as

$$\tau_{ext} = \frac{4}{D}\left(\frac{L}{\pi}\right)^2. \quad \text{(Equation 10)}$$

This time parameter is almost independent to the bias voltage as long as the carrier transport mechanism within the bulk absorber is significantly changed. According to the semiconductor theory,[64] the carrier recombination within the absorber can be modulated through the bias voltage by changing the carrier density or the density of defect crossing with the Fermi energy level, which yields an approximate relationship of

$$\tau_R = \tau_{R0} e^{-\frac{qV}{AK_BT}} = \frac{1}{\sigma v_{th} N_t} e^{-\frac{qV}{AK_BT}}, \quad \text{(Equation 11)}$$

where σ is the charge trapping cross-section that can be estimated by a variety of experiments, v_{th} is the thermal velocity calculated from the carrier effective mass, N_t is the defect density, and A is a fitting factor that can be used to reflect the mechanism of bias voltage-dependent carrier recombination.

When A is between 1 and 2, the increase in charge recombination under higher voltage should arise from the increase in carrier density. When A is larger than 2, we may need to consider the Fermi energy-level-dependent defect density.

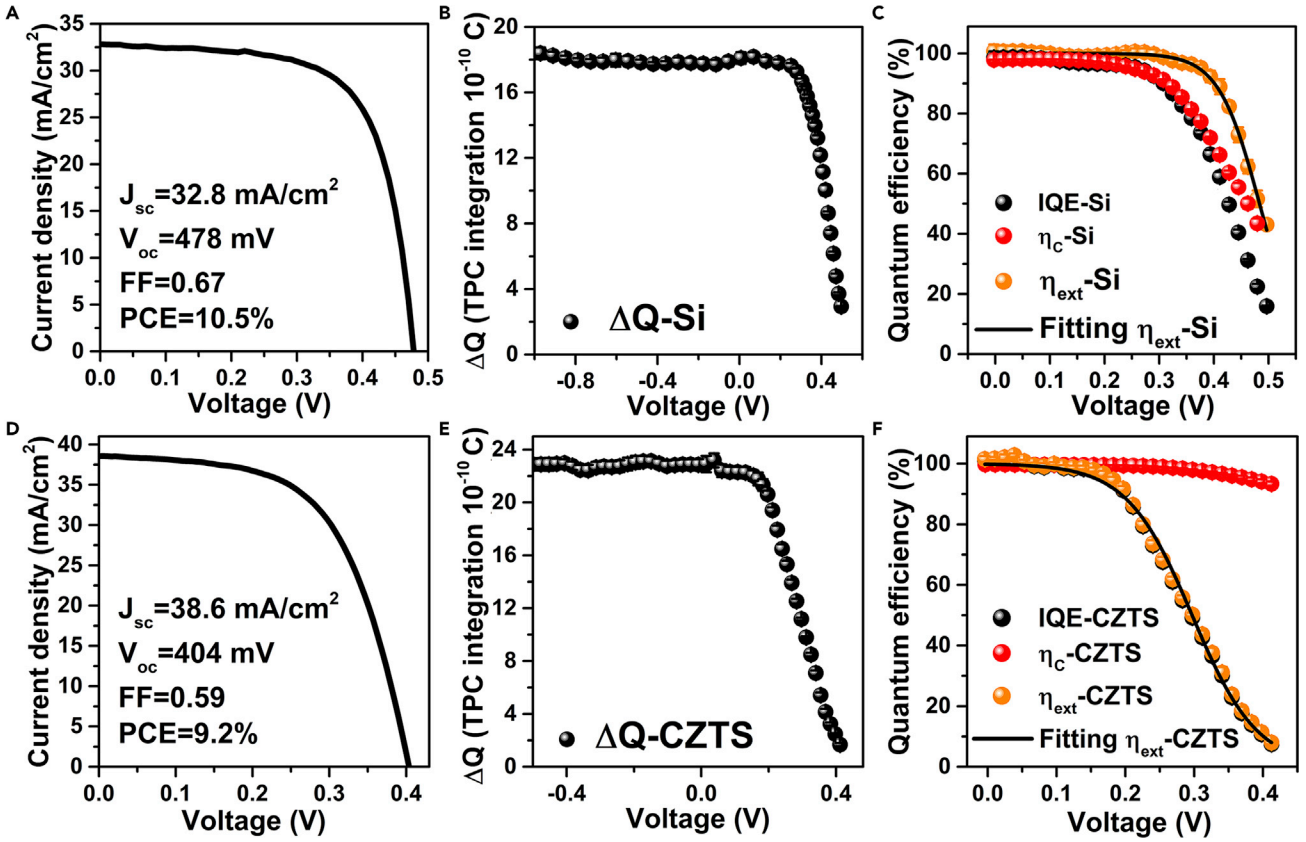

Figure 6. Electrical Transients Study of a Commercial Polycrystalline Silicon and Lab-Made CZTS Solar Cells

(A–F) Representative *I-V* curves of the cells (A and D). The relationship between the TPC integrated charge and the bias voltage (B and E). The bias voltage-dependent IQE (black sphere), η_C (red sphere), and η_{ext} (orange sphere) (C and F). Black lines are the fitting of the η_{ext} curve. Error bars in (B), (C), (E), and (F), statistical standard deviation of a batch of cells.

Combining Equations 10 and 11 into Equation 9, we can then obtain the theoretical relationship between η_{ext} and voltage, that is:

$$\eta_{ext} = \left[1 + \frac{4\sigma v_{th} N_t}{D}\left(\frac{L}{\pi}\right)^2 \exp\left(\frac{qV}{AK_BT}\right)\right]^{-1}. \qquad \text{(Equation 12)}$$

In the following, we will use these theoretical results to study the charge loss mechanisms and defect density of the polycrystalline silicon, $Cu_2ZnSn(S, Se)_4$ (CZTS) and perovskite solar cells and to demonstrate the reliability of this new analysis method.

The application of this methodology to a silicon solar cell is presented in Figures 6A–6C. This commercial silicon solar cell was directly used and gives a PCE of 10.5% (Figure 6A). The TPC integration (ΔQ (V)) was firstly obtained at different voltages (Figure 6B) and then used to derive the IQE (Figure 6C). The IQE exhibits a similar voltage-dependent behavior to that of the *I-V* curve. Using both TPC and TPV, the η_C (V) was calculated, which decreased obviously when the voltage was higher than 0.3 V. Further, the η_{ext} was derived from Equation 8. From 0.3 to 0.45 V, the η_{ext} is clearly larger than the η_C, which implies that the charge loss in this cell mainly occurs at the n^+-p silicon or the electrode interface. Usually, a surface or interface passivation by silicon oxides can suppress this interface backward recombination. According to Equation 12, the η_{ext} (V) is fitted by using the previously reported σ and D,[65,66] yielding N_t of 4.75×10^{12} cm^{-3}. This value is in the similar order of

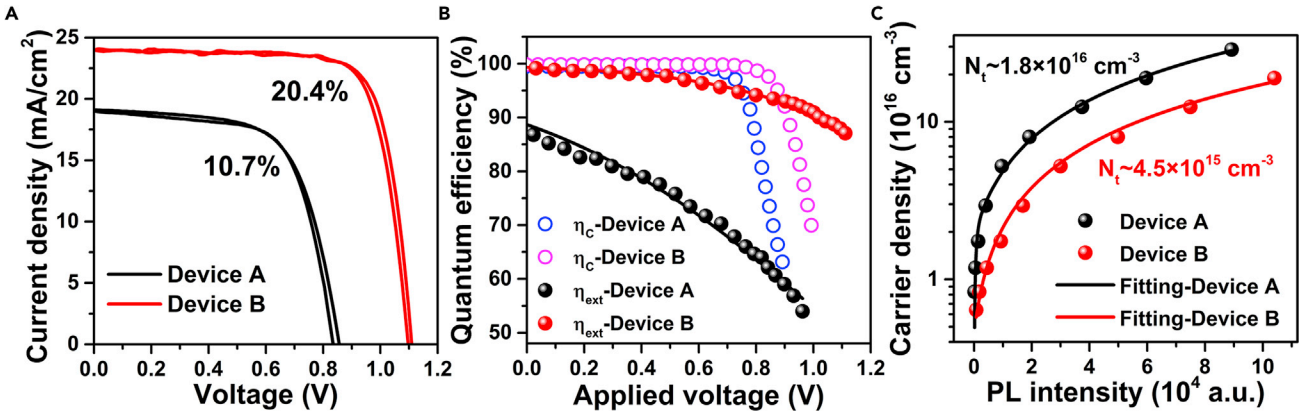

Figure 7. Electrical Transients Study of Perovskite Solar Cells

(A) The representative *I-V* curves of device A and B, which were fabricated with different perovskite deposition conditions.

(B) Voltage-dependent η_C and η_{ext} for these two devices.

(C) The relationships between PL intensity and photoexcited carrier density for different perovskite films. The solid lines are numerical fits with the trap density model.

magnitude to the defect density of polycrystalline silicon material measured by other methods,[67,68] demonstrating the reliability of the electrical transient methodology proposed here.

For the CZTS solar cell, a different charge loss behavior is found, as presented in Figures 6D–6F. Its η_C keeps higher than 90% across the studied voltage range, whereas its η_{ext} drops obviously at voltages higher than 0.2 V. This means that severe charge loss and low V_{OC} issue that this cell encounters mainly arises from the bulk recombination. These results agree with recent findings that the CZTS absorber possesses complicated defect properties.[69] Since the η_{ext} of the CZTS cell can be well described by our model, we infer that the width of built-in electric field is much smaller than the absorber thickness and the electric field is too weak to drive effective drift transport. Thus, for improving the CZTS performance, defect and heterojunction engineering is needed. The defect density is further estimated to be 2.1×10^{15} cm^{-3}, also in a similar order of magnitude to that measured by other methods.[70]

This method is further used to study the charge loss of the perovskite solar cell. The perovskite absorber of device A (P-A) was deposited by a conventional one-step spin-coating method without any anti-solvent, which usually possesses a higher defect density and thus exhibits a low PCE of 10.7%. The perovskite absorber of device B (P-B) was deposited by the widely used anti-solvent method, contributing to a high PCE of 20.4%. For these two cells, SnO_2 nanoparticle film was used as the ETL and the hysteresis was negligible. The short-circuit current density (J_{SC}), V_{OC} and fill factor (FF) of device A were all much lower than that of device B. The η_C (V) and η_{ext} (V) were derived from the m-TPC-TPV to discriminate the charge loss mechanisms, especially that of device A. As in Figure 7B, these two cells possess a high η_C approaching 100% at voltages lower than 0.8 V, which indicates that charge loss through the backward recombination at the ETL and HTL-perovskite interface in both devices is negligible at low voltages. This means that shunt contacts between the ETL and HTL due to the incomplete coverage of the perovskite film that may appear in the conventional spin coting method does not dominate the charge loss of the cells here. For device A, its η_C begins to decrease obviously from 0.8 V while η_C of device B begins to decrease at ~0.9 V. For device B, the η_C at high voltages still

Table 1. Device Performance and Derived Defect Density of the Studied Cells

Cell	J_{SC} (mA cm^{-2})	V_{OC} (V)	FF	PCE (%)	σ (cm^2)	D (cm^{2}s^{-1})	A	N_t (cm^{-3})	
								ET	PL
Si	32.8	0.48	0.67	10.5	6.0×10^{-21}[65]	~40[66]	1.7	4.8×10^{12}	–
CZTS	38.6	0.40	0.59	9.2	3.5×10^{-17}[70]	~1.0[73]	1.8	2.1×10^{15}	–
P–A	19.0	0.84	0.67	10.7	1.0×10^{-17}	~0.027	20.1	4.3×10^{15}	1.8×10^{16}
P–B	23.9	1.11	0.77	20.4	2.3×10^{-16}	~0.040	13.0	1.5×10^{15}	4.5×10^{15}

need to be further improved to boost its current V_{OC}, which may be determined by the interface energy level structures and charge recombination. It is suggested that this is the key mechanism for the charge loss of the currently reported highest efficient perovskite solar cells.

The origin for the device performance difference mainly lies in the $\eta_{ext}(V)$. In the SC condition, the η_{ext} for device A is only ~86% while device B exhibits a high η_{ext} of 99%. This makes a great contribution to the J_{SC} difference and indicates that charge loss of device A mainly occurs in the perovskite absorber. Further according to Equation 12 and the experimentally measured σ, D, and L (see Figures S1–S3 and Experimental Procedures), the defect density of the perovskite absorber in device A is estimated to be ~4.3×10^{15} cm^{-3}, which is about three times as high as that of device B. These values obtained by the electrical transient method (ET) are approximately two orders of magnitude lower than that measured from thermal admittance spectroscopy.[71,72] This may arise because not all the defects probed by the capacitance response could make contribution to the bulk charge recombination. Interface defects induced by the ion migration may also influence the accurate measurement of bulk defect. For a more reasonable comparison, we used excitation-intensity-dependent photoluminescence to estimate the perovskite defect density (see Experimental Procedures),[26] as presented in Figure 7C and Table 1. The result is in the similar order of magnitude to that obtained by the ET method.

More interestingly, we find that the fitted A for the perovskite solar cell is much higher than 2, indicating that the bulk recombination is not sensitive to the bias voltage. This may arise from two possible reasons, that is, (1) ion migration has screened the influence of bias voltage on the bulk perovskite[74] or (2) the distinctive defect distribution of the perovskite has influenced the dependence of carrier recombination lifetime to the bias voltage.[75] To check these possibilities, the defect analysis was further carried out on $MAPbBr_3$-based cell because these two types of perovskite should possess similar defect distribution properties but significantly different ion migration behaviors. It is found that the $MAPbBr_3$ cell exhibits a much smaller A of ~5.2 (see Figure S4 and Experimental Procedures). This result helps us to attribute the large A observed for device A and B to the screening effect of ion migration.

DISCUSSION

In summary, this work has comprehensively revealed how to exploit electrical transients for a quantitative study of charge loss within photovoltaic devices. A more accurate evaluation of voltage-dependent differential capacitances together with a clear description of the photovoltage establishing process is put forward to verify the unreasonability of the previously widely used tail-state framework. Alternatively, we provide a new way to quantifying charge loss and defect density of solar cells by

electrical transients. Quantum efficiency of charge transfer at different interfaces (i.e., η_C and η_{ext}) can be extracted to reveal the charge loss mechanisms of a solar cell; moreover, the defect density of the light absorber is also measured from the η_{ext}-voltage behaviors. This new method has been successfully applied to the polycrystalline silicon, CZTS, and perovskite solar cells. More importantly, this methodology is supposed to be applicable to other semiconductor energy devices with similar structures, such as the CIGS and Sb_2Se_3 planar junction solar cells. Therefore, our work provides a more accurate understanding toward dynamic physics processes and charge loss mechanisms of solar cells and other related semiconductor energy devices with the aid of electrical transient techniques. It makes a great step forward to exploring the essential properties of solar cells, giving inspirations for solving the crucial issues and having values for developing other semiconductor materials and devices.

EXPERIMENTAL PROCEDURES

Materials

PbI_2 (99.9985%) and SnO_2 colloidal dispersion (tin (IV) oxide, 15% in H_2O colloidal dispersion) were obtained from Alfa Asear. $PbBr_2$ (99.999%) was obtained from Sigma-Aldrich. Methylammonium bromide (MABr), methylammonium iodide (MAI), and formamidinium iodide (FAI) were obtained from Xi'an Polymer Light Technology Corp. N,N-Dimethylformamide (DMF), dimethylsulfoxide (DMSO), chlorobenzene, and tert-butylpyridine (TBP, 99.999%) were obtained from Alfa Aesar. Spiro-OMeTAD was obtained from Luminescence Technology Corp. (Lumtec). Bis(trifluoromethane)sulfonimide lithium salt (LiTFSI) was purchased from Sigma-Aldrich (99.9985%) and tris(2-(1H-pyrazol-1-yl)-4-tert-butylpyridine)-cobalt(III) tris(bis (trifluorom- ethylsulfonyl)imide) (FK209) was from Dyesol.

Device Fabrication

Laser-patterned ITO glass (sheet resistance = 15 Ω per square) was pre-cleaned in an ultrasonic bath using soap water, deionized water, acetone, and ethanol for 30 min each and treated in an ultraviolet–ozone chamber for 15 min. A thin layer of SnO_2 nanoparticles was spin coated onto the pre-cleaned ITO substrate using a SnO_2 colloidal dispersion solution in water (6.18%) at 5,000 rpm for 30 s and annealed at 150°C for 30 min in ambient atmosphere. [6,6]-phenyl-C61-butyric acid (PCBA, 0.1 mg/mL) in chlorobenzene was spin coated on the top of SnO_2 film.[76] The precursor solution for perovskite films was prepared by dissolving PbI_2 (1.32 M), $PbBr_2$ (0.12 M), FAI (1.08 M), MAI (0.12 M), and MABr (0.24 M) in DMF-DMSO mixed solvent (v:v = 4:1) and stirred overnight at room temperature. The perovskite film was spin coated by an anti-solvent one-step method in the glove box. The perovskite precursor solution was spin coated at 1,000 rpm for 10 s and 5,000 rpm for 30 s, chlorobenzene (120 μL) was poured onto the substrate at 15 s during the high-speed stage. Then the half-crystallization film was heated at 150°C in the glove box for 10 min and 100°C in vacuum for 40 min. Then, a 200-nm-thick spiro-OMeTAD layer was deposited by spin coating at 3,500 rpm for 30 s and then heated for 10 min at 60°C on the top of perovskite films. The spiro-OMeTAD solution was prepared by dissolving in chlorobenzene (60 mM) with the additives of Li-TFSI, FK209, and TBP at doping molar ratios of 0.5, 0.03, and 3.3. Finally, 80-nm-thick Au electrodes were deposited via thermal evaporation at an atmospheric pressure of 10^{-7} Torr (Kurt J. Lesker). The multicrystalline silicon solar cell was directly purchased from Stark Electronics, China. The CZTS solar cells were fabricated based on our previous work.[77]

Characterization

J-V characteristics were measured under AM 1.5 simulated sunlight (100 mW/cm^2) from Zolix SS150A, which was recorded by a digital source meter (Keithley model 2602). External quantum efficiency (EQE) of the devices was measured with a lab-made setup under 0.3–0.9 mW/cm^2 monochromic light illumination. The wavelength was from 300 to 850 nm. Light intensity-dependent I_{SC} and V_{OC} curves were performed by the lab-made instrument mainly using an intensity tunable light emitting diode (Nanjin Hongzhao, S3000) and an IM6ex electrochemical workstation (Zahner). Modulated transient photocurrent and photovoltage (m-TPC-TPV) measurements were obtained by a tunable nanosecond laser (Opotek, RADIANT 532 LD) pumped at 532 nm and recorded by a sub-nanosecond resolved digital oscilloscope (Tektronix, MDO3034) with input impedances of 50 Ω or 1 MΩ, respectively. A signal generator (Tektronix, AFG3052C) together with a low-pass filter was applied to give steady-state bias voltages over the cell. Traditional V_{OC}-TPC-TPV measurements were obtained by a tunable nanosecond laser (Opotek, RADIANT 532 LD) pumped at 532 nm and recorded by a sub-nanosecond resolved digital oscilloscope (Tektronix, MDO3034) with input impedances of 50 Ω or 1 MΩ, respectively. The background illumination was provided by an intensity tunable light emitting diode (Nanjin Hongzhao, S3000). The intensity was first calibrated to the J_{SC} of devices measured under AM1.5 solar simulator. Time-resolved photoluminescence (TRPL) was measured by the PL spectrometer (Edinburgh Instruments, FLS900) using a pulsed diode laser (EPL-445, ~20 nJ·cm^{-2}/pulse) as the excitation source. The thickness of the perovskite films was measured by the cross-sectional SEM image as well as a surface profiler (KLA-Tencor). Thermal admittance spectroscopy was performed using an IM6ex electrochemical workstation (Zahner), in which the scanning frequency was set between 0.1 and 10^5 Hz, and the amplitude of the sine perturbation bias was set to 10 mV.

SUPPLEMENTAL INFORMATION

Supplemental Information can be found online at https://doi.org/10.1016/j.joule.2019.12.016.

ACKNOWLEDGMENTS

This work was supported by the Natural Science Foundation of China (nos. 51627803, 51421002, 91733301, 51761145042, 53872321, 51572288, and 11874402), the International Partnership Program of Chinese Academy of Sciences (no. 112111KYSB20170089), and the National Key R&D Program of China (no. 2018YFB1500101).

AUTHOR CONTRIBUTIONS

Y.L., J.S., and Q.M. conceived the idea. Y.L. did device fabrication, electric circuit construction, electrical transient and other measurements, and theoretical simulation. J.S. proposed the device model, electric circuit model, and experimental designs. Y.L. and J.S. did the data analysis. B.Y., B.D., J.W., and H.L. participated in the device fabrications and some material and device characterizations. D.L, Y.L., and H.W. supported the measurement system construction, device fabrication, characterizations, and discussions. Y.L., J.S., and Q.M. participated in manuscript writing and revising. J.S. and D.L. polished the manuscript language. All authors were involved in the discussions and approved the manuscript. Y.L. and J.S. have contributed equally to this work.

DECLARATION OF INTERESTS

The authors declare no competing interests.

Received: September 6, 2019
Revised: November 11, 2019
Accepted: December 18, 2019
Published: January 29, 2020

REFERENCES

1. Benka, S.G. (2002). The energy challenge. Phys. Today *55*, 38–39.
2. Luque, A., and Hegedus, S. (2011). Handbook of Photovoltaic Science and Engineering, Second Edition (John Wiley & Sons).
3. Gray, P.R., Hurst, P.J., Lewis, S.H., and Meyer, R.G. (2009). Analysis and Design of Analog Integrated Circuits, Fifth Edition (John Wiley & Sons).
4. Rabaey, J.M. (1996). Digital Integrated Circuits (Prentice-Hall).
5. Yang, Y., Ostrowski, D.P., France, R.M., Zhu, K., Lagemaat, J., Luther, J.M., and Beard, M.C. (2016). Observation of a hot-phonon bottleneck in lead-iodide perovskites. Nat. Photon. *10*, 53–59.
6. Fu, J., Xu, Q., Han, G., Wu, B., Huan, C.H.A., Leek, M.L., and Sum, T.C. (2017). Hot carrier cooling mechanisms in halide perovskites. Nat. Commun. *8*, 1300.
7. Zhu, H., Miyata, K., Fu, Y., Wang, J., Joshi, P.P., Niesner, D., Williams, K.W., Jin, S., and Zhu, X.Y. (2016). Screening in crystalline liquids protects energetic carriers in hybrid perovskites. Science *353*, 1409–1413.
8. Yang, J., Wen, X., Xia, H., Sheng, R., Ma, Q., Kim, J., Tapping, P., Harada, T., Kee, T.W., Huang, F., et al. (2017). Acoustic-optical phonon up-conversion and hot-phonon bottleneck in lead-halide perovskites. Nat. Commun. *8*, 14120.
9. Leijtens, T., Eperon, G.E., Noel, N.K., Habisreutinger, S.N., Petrozza, A., and Snaith, H.J. (2015). Stability of metal halide perovskite solar cells. Adv. Energy Mater. *5*, 1500963.
10. Meloni, S., Moehl, T., Tress, W., Franckevičius, M., Saliba, M., Lee, Y.H., Gao, P., Nazeeruddin, M.K., Zakeeruddin, S.M., Rothlisberger, U., et al. (2016). Ionic polarization-induced current–voltage hysteresis in $CH_3NH_3PbX_3$ perovskite solar cells. Nat. Commun. *7*, 10334.
11. Chen, B., Zheng, X., Yang, M., Zhou, Y., Kundu, S., Shi, J., Zhu, K., and Priya, S. (2015). Interface band structure engineering by ferroelectric polarization in perovskite solar cells. Nano Energy *13*, 582–591.
12. Li, C., Tscheuschner, S., Paulus, F., Hopkinson, P.E., Kießling, J., Köhler, A., Vaynzof, Y., and Huettner, S. (2016). Iodine migration and its effect on hysteresis in perovskite solar cells. Adv. Mater. *28*, 2446–2454.
13. Shao, Y., Fang, Y., Li, T., Wang, Q., Dong, Q., Deng, Y., Yuan, Y., Wei, H., Wang, M., Gruverman, A., et al. (2016). Grain boundary dominated ion migration in polycrystalline organic-inorganic halide perovskite films. Energy Environ. Sci. *9*, 1752–1759.
14. Domanski, K., Roose, B., Matsui, T., Saliba, M., Turren-Cruz, S.H., Correa-Baena, J.P., Carmona, C.R., Richardson, G., Foster, J.M., De Angelis, F., et al. (2017). Migration of cations induces reversible performance losses over day/night cycling in perovskite solar cells. Energy Environ. Sci. *10*, 604–613.
15. Correa-Baena, J.P., Saliba, M., Buonassisi, T., Grätzel, M., Abate, A., Tress, W., and Hagfeldt, A. (2017). Promises and challenges of perovskite solar cells. Science *358*, 739–744.
16. Shi, J., Li, Y., Li, Y., Li, D., Luo, Y., Wu, H., and Meng, Q. (2018). From ultrafast to ultraslow: charge-carrier dynamics of perovskite solar cells. Joule *2*, 879–901.
17. Zhu, Z., Ma, J., Wang, Z., Mu, C., Fan, Z., Du, L., Bai, Y., Fan, L., Yan, H., Phillips, D.L., and Yang, S. (2014). Efficiency enhancement of perovskite solar cells through fast electron extraction: the role of graphene quantum dots. J. Am. Chem. Soc. *136*, 3760–3763.
18. Guo, Z., Wan, Y., Yang, M., Snaider, J., Zhu, K., and Huang, L. (2017). Long-range hot-carrier transport in hybrid perovskites visualized by ultrafast microscopy. Science *356*, 59–62.
19. Piatkowski, P., Cohen, B., Ponseca, C.S., Jr., Salado, M., Kazim, S., Ahmad, S., Sundström, V., and Douhal, A. (2016). Unraveling charge carriers generation, diffusion, and recombination in formamidinium lead triiodide perovskite polycrystalline thin film. J. Phys. Chem. Lett. *7*, 204–210.
20. Valverde-Chávez, D.A., Ponseca, C.S., Jr., Stoumpos, C.C., Yartsev, A., Kanatzidis, M.G., Sundström, V., and Cooke, D.G. (2015). Intrinsic femtosecond charge generation dynamics in single crystal $CH_3NH_3PbI_3$. Energy Environ. Sci. *8*, 3700–3707.
21. Wehrenfennig, C., Liu, M., Snaith, H.J., Johnston, M.B., and Herz, L.M. (2014). Charge-carrier dynamics in vapour-deposited films of the organolead halide perovskite $CH_3NH_3PbI_{3-x}Cl_x$. Energy Environ. Sci. *7*, 2269–2275.
22. Xing, G., Mathews, N., Sun, S., Lim, S.S., Lam, Y.M., Grätzel, M., Mhaisalkar, S., and Sum, T.C. (2013). Long-range balanced electron- and hole-transport lengths in organic-inorganic $CH_3NH_3PbI_3$. Science *342*, 344–347.
23. Stranks, S.D., Eperon, G.E., Grancini, G., Menelaou, C., Alcocer, M.J., Leijtens, T., Herz, L.M., Petrozza, A., and Snaith, H.J. (2013). Electron-hole diffusion lengths exceeding 1 micrometer in an organometal trihalide perovskite absorber. Science *342*, 341–344.
24. Stranks, S.D., Burlakov, V.M., Leijtens, T., Ball, J.M., Goriely, A., and Snaith, H.J. (2014). Recombination kinetics in organic-inorganic perovskites: excitons, free charge, and subgap states. Phys. Rev. Appl. *2*, 034007.
25. Yamada, Y., Nakamura, T., Endo, M., Wakamiya, A., and Kanemitsu, Y. (2014). Photocarrier recombination dynamics in perovskite $CH_3NH_3PbI_3$ for solar cell applications. J. Am. Chem. Soc. *136*, 11610–11613.
26. Li, Y., Li, Y., Shi, J., Zhang, H., Wu, J., Li, D., Luo, Y., Wu, H., and Meng, Q. (2018). High quality perovskite crystals for efficient film photodetectors induced by hydrolytic insulating oxide substrates. Adv. Funct. Mater. *28*, 1705220.
27. Ponseca, C.S., Savenije, T.J., Abdellah, M., Zheng, K., Yartsev, A., Pascher, T., Harlang, T., Chabera, P., Pullerits, T., Stepanov, A., et al. (2014). Organometal halide perovskite solar cell materials rationalized: ultrafast charge generation, high and microsecond-long balanced mobilities, and slow recombination. J. Am. Chem. Soc. *136*, 5189–5192.
28. Oga, H., Saeki, A., Ogomi, Y., Hayase, S., and Seki, S. (2014). Improved understanding of the electronic and energetic landscapes of perovskite solar cells: high local charge carrier mobility, reduced recombination, and extremely shallow traps. J. Am. Chem. Soc. *136*, 13818–13825.
29. Guo, D., Caselli, V.M., Hutter, E.M., and Savenije, T.J. (2019). Comparing the calculated fermi level splitting with the open-circuit voltage in various perovskite cells. ACS Energy Lett. *4*, 855–860.
30. Kiermasch, D., Baumann, A., Fischer, M., Dyakonov, V., and Tvingstedt, K. (2018). Revisiting lifetimes from transient electrical characterization of thin film solar cells; a capacitive concern evaluated for silicon, organic and perovskite devices. Energy Environ. Sci. *11*, 629–640.
31. Du, T., Kim, J., Ngiam, J., Xu, S., Barnes, P.R.F., Durrant, J.R., and McLachlan, M.A. (2018). Elucidating the origins of subgap tail states and open-circuit voltage in methylammonium lead triiodide perovskite solar cells. Adv. Funct. Mater. *28*, 1801808.
32. Wheeler, S., Bryant, D., Troughton, J., Kirchartz, T., Watson, T., Nelson, J., and Durrant, J.R. (2017). Transient optoelectronic analysis of the impact of material energetics and recombination kinetics on the open-circuit voltage of hybrid perovskite solar cells. J. Phys. Chem. C *121*, 13496–13506.

33. Shi, J., Li, D., Luo, Y., Wu, H., and Meng, Q. (2016). Opto-electro-modulated transient photovoltage and photocurrent system for investigation of charge transport and recombination in solar cells. Rev. Sci. Instrum. *87*, 123107.

34. Shi, J., Zhang, H., Xu, X., Li, D., Luo, Y., and Meng, Q. (2016). Microscopic charge transport and recombination processes behind the photoelectric hysteresis in perovskite solar cells. Small *12*, 5288–5294.

35. Shi, J., Xu, X., Zhang, H., Luo, Y., Li, D., and Meng, Q. (2015). Intrinsic slow charge response in the perovskite solar cells: electron and ion transport. Appl. Phys. Lett. *107*, 163901.

36. Wood, S., Blakesley, J.C., and Castro, F.A. (2018). Assessing the validity of transient photovoltage measurements and analysis for organic solar cells. Phys. Rev. Appl. *10*, 024038.

37. Sandberg, O.J., Tvingstedt, K., Meredith, P., and Armin, A. (2019). Theoretical perspective on transient photovoltage and charge extraction techniques. J. Phys. Chem. C *123*, 14261–14271.

38. Di Giulio, M.O., Galassini, S., Micocci, G., Tepore, A., and Manfredotti, C. (1981). Determination of minority-carrier lifetime in silicon solar cells from laser-transient photovoltaic effect. J. Appl. Phys. *52*, 7219–7223.

39. Sang, Y., Liu, W., Qiao, F., Kang, D., and Liu, A. (2013). Transient photovoltage in poly(3-hexylthiophene)/n-crystalline-silicon heterojunction. Vacuum *93*, 28–30.

40. Wang, X., Karanjit, S., Zhang, L., Fong, H., Qiao, Q., and Zhu, Z. (2011). Transient photocurrent and photovoltage studies on charge transport in dye sensitized solar cells made from the composites of TiO_2 nanofibers and nanoparticles. Appl. Phys. Lett. *98*, 082114.

41. Enache-Pommer, E., Boercker, J.E., and Aydil, E.S. (2007). Electron transport and recombination in polycrystalline TiO_2 nanowire dye-sensitized solar cells. Appl. Phys. Lett. *91*, 123116.

42. Pang, S., Cheng, K., Yuan, Z., Xu, S., Cheng, G., and Du, Z. (2014). Study on dynamics of photoexcited charge injection and trapping in CdS quantum dots sensitized TiO_2 nanowire array film electrodes. Appl. Phys. Lett. *104*, 201601.

43. Li, C.Z., Chang, C.Y., Zang, Y., Ju, H.X., Chueh, C.C., Liang, P.W., Cho, N., Ginger, D.S., and Jen, A.K.Y. (2014). Suppressed charge recombination in inverted organic photovoltaics via enhanced charge extraction by using a conductive fullerene electron transport layer. Adv. Mater. *26*, 6262–6267.

44. O'Regan, B.C., Scully, S., Mayer, A.C., Palomares, E., and Durrant, J.R. (2005). The effect of Al_2O_3 barrier layers in TiO_2/dye/CuSCN photovoltaic cells explored by recombination and DOS characterization using transient photovoltage measurements. J. Phys. Chem. B *109*, 4616–4623.

45. Shuttle, C.G., O'Regan, B., Ballantyne, A.M., Nelson, J., Bradley, D.D.C., de Mello, J., and Durrant, J.R. (2008). Experimental determination of the rate law for charge carrier decay in a polythiophene: fullerene solar cell. Appl. Phys. Lett. *92*, 093311.

46. Maurano, A., Shuttle, C.G., Hamilton, R., Ballantyne, A.M., Nelson, J., Zhang, W., Heeney, M., and Durrant, J.R. (2011). Transient optoelectronic analysis of charge carrier losses in a selenophene/fullerene blend solar cell. J. Phys. Chem. C *115*, 5947–5957.

47. Marlow, F., Hullermann, A., and Messmer, L. (2015). Is the charge transport in dye-sensitized solar cells really understood? Adv. Mater. *27*, 2447–2452.

48. Shao, Y., Yuan, Y., and Huang, J. (2016). Correlation of energy disorder and open-circuit voltage in hybrid perovskite solar cells. Nat. Energy *1*, 15001.

49. Zohar, A., Kulbak, M., Levine, I., Hodes, G., Kahn, A., and Cahen, D. (2019). What limits the open-circuit voltage of bromide perovskite-based solar cells? ACS Energy Lett. *4*, 1–7.

50. Wright, A.D., Milot, R.L., Eperon, G.E., Snaith, H.J., Johnston, M.B., and Herz, L.M. (2017). Band-tail recombination in hybrid lead iodide perovskite. Adv. Funct. Mater. *27*, 1700860.

51. Wu, J., Shi, J., Li, Y., Li, H., Wu, H., Luo, Y., Li, D., and Meng, Q. (2019). Quantifying the interface defect for the stability origin of perovskite solar cells. Adv. Energy Mater. *9*, 1901352.

52. Li, Y., Li, Y., Shi, J., Li, H., Zhang, H., Wu, J., Li, D., Luo, Y., Wu, H., and Meng, Q. (2018). Photocharge accumulation and recombination in perovskite solar cells regarding device performance and stability. Appl. Phys. Lett. *112*, 053904.

53. Stolterfoht, M., Caprioglio, P., Wolff, C.M., Márquez, J.A., Nordmann, J., Zhang, S., Rothhardt, D., Hörmann, U., Amir, Y., Redinger, A., et al. (2019). The impact of energy alignment and interfacial recombination on the internal and external open-circuit voltage of perovskite solar cells. Energy Environ. Sci. *12*, 2778–2788.

54. Schelhas, L.T., Li, Z., Christians, J.A., Goyal, A., Kairys, P., Harvey, S.P., Kim, D.H., Stone, K.H., Luther, J.M., Zhu, K., et al. (2019). Insights into operational stability and processing of halide perovskite active layers. Energy Environ. Sci. *12*, 1341–1348.

55. Liu, X., Du, X., Wang, J., Duan, C., Tang, X., Heumueller, T., Liu, G., Li, Y., Wang, Z., Wang, J., et al. (2018). Efficient organic solar cells with extremely high open-circuit voltages and low voltage losses by suppressing nonradiative recombination losses. Adv. Energy Mater. *8*, 1801699.

56. Tress, W., Yavari, M., Domanski, K., Yadav, P., Niesen, B., Correa Baena, J.P.C., Hagfeldt, A., and Graetzel, M. (2018). Interpretation and evolution of open-circuit voltage, recombination, ideality factor and subgap defect states during reversible light-soaking and irreversible degradation of perovskite solar cells. Energy Environ. Sci. *11*, 151–165.

57. Caprioglio, P., Stolterfoht, M., Wolff, C.M., Unold, T., Rech, B., Albrecht, S., and Neher, D. (2019). On the relation between the open-circuit voltage and quasi-fermi level splitting in efficient perovskite solar cells. Adv. Energy Mater. *9*, 1901631.

58. Bisquert, J., Zaban, A., Greenshtein, M., and Mora-Seró, I. (2004). Determination of rate constants for charge transfer and the distribution of semiconductor and electrolyte electronic energy levels in dye-sensitized solar cells by open-circuit photovoltage decay method. J. Am. Chem. Soc. *126*, 13550–13559.

59. Martínez-Ferrero, E., Seró, I.M., Albero, J., Giménez, S., Bisquert, J., and Palomares, E. (2010). Charge transfer kinetics in CdSe quantum dot sensitized solar cells. Phys. Chem. Chem. Phys. *12*, 2819–2821.

60. Pazoki, M., Cappel, U.B., Johansson, E.M.J., Hagfeldt, A., and Boschloo, G. (2017). Characterization techniques for dye-sensitized solar cells. Energy Environ. Sci. *10*, 672–709.

61. Listorti, A., O'Regan, B.C., and Durrant, J.R. (2011). Electron transfer dynamics in dye-sensitized solar cells. Chem. Mater. *23*, 3381–3399.

62. Courtier, N.E., Cave, J.M., Foster, J.M., Walker, A.B., and Richardson, G. (2019). How transport layer properties affect perovskite solar cell performance: insights from a coupled charge transport/ion migration model. Energy Environ. Sci. *12*, 396–409.

63. Sproul, A.B. (1994). Dimensionless solution of the equation describing the effect of surface recombination on carrier decay in semiconductors. J. Appl. Phys. *76*, 2851–2854.

64. Sze, S.M., and Ng, K.K. (2007). Physics of Semiconductor Devices, Third edition (John Wiley & Sons).

65. Criado, A., Alonso, B., and Piqueras, J. (1978). Deep traps in polysilicon solar cells. Electron. Lett. *14*, 622–623.

66. Martinez, J., Alonso, B., Criado, A., and Piqueras, J. (1976). Solar cells from polysilicon rods. Electron. Lett. *12*, 671–672.

67. Datta, A., Damon-Lacoste, J., Roca i Cabarrocas, P.R., and Chatterjee, P. (2008). Defect states on the surfaces of a P-type c-Si wafer and how they control the performance of a double heterojunction solar cell. Sol. Energy Mater. Sol. Cells *92*, 1500–1507.

68. Park, Y., Lu, J., Park, J.H., and Rozgonyi, G. (2015). Impact of structural defect density on gettering of transition metal impurities during phosphorus emitter diffusion in multi-crystalline silicon solar cell processing. Electron. Mater. Lett. *11*, 658–663.

69. Pal, K., Singh, P., Bhaduri, A., and Thapa, K.B. (2019). Current challenges and future prospects for a highly efficient (>20%) kesterite CZTS solar cell: a review. Sol. Energ Mater. Sol. Cells *196*, 138–156.

70. Duan, H.S., Yang, W., Bob, B., Hsu, C.J., Lei, B., and Yang, Y. (2013). The role of sulfur in solution-processed $Cu_2ZnSn(S,Se)_4$ and its effect on defect properties. Adv. Funct. Mater. *23*, 1466–1471.

71. Xing, G., Mathews, N., Lim, S.S., Yantara, N., Liu, X., Sabba, D., Grätzel, M., Mhaisalkar, S.,

and Sum, T.C. (2014). Low-temperature solution-processed wavelength-tunable perovskites for lasing. Nat. Mater. *13*, 476–480.

72. Adinolfi, V., Peng, W., Walters, G., Bakr, O.M., and Sargent, E.H. (2018). The electrical and optical properties of organometal halide perovskites relevant to optoelectronic performance. Adv. Mater. *30*, 29024039.

73. Gokmen, T., Gunawan, O., and Mitzi, D.B. (2013). Minority carrier diffusion length extraction in $Cu_2ZnSn(Se,S)_4$ solar cells. J. Appl. Phys. *114*, 114511.

74. Belisle, R.A., Nguyen, W.H., Bowring, A.R., Calado, P., Li, X., Irvine, S.J.C., McGehee, M.D., Barnes, P.R.F., and O'Regan, B.C. (2017). Interpretation of inverted photocurrent transients in organic lead halide perovskite solar cells: proof of the field screening by mobile ions and determination of the space charge layer widths. Energy Environ. Sci. *10*, 192–204.

75. Shi, J., Zhang, H., Li, Y., Jasieniak, J.J., Li, Y., Wu, H., Luo, Y., Li, D., and Meng, Q. (2018). Identification of high-temperature exciton states and their phase-dependent trapping behaviour in lead halide perovskites. Energy Environ. Sci. *11*, 1460–1469.

76. Dong, Y., Li, W., Zhang, X., Xu, Q., Liu, Q., Li, C., and Bo, Z. (2016). Highly efficient planar perovskite solar cells via interfacial modification with fullerene derivatives. Small *12*, 1098–1104.

77. Duan, B., Guo, L., Yu, Q., Shi, J., Wu, H., Luo, Y., Li, D., Wu, S., Zheng, Z., and Meng, Q. (2020). Highly efficient solution-processed CZTSSe solar cells based on a convenient sodium-incorporated post-treatment method. J. Energy Chem. *40*, 196–203.